



Published in final edited form as:

Opt Lett. 2014 February 1; 39(3): 430–433.

Spatially Fourier-encoded photoacoustic microscopy using a digital micromirror device

Jinyang Liang, Liang Gao, Chiye Li, and Lihong V. Wang*

Optical Imaging Laboratory, Department of Biomedical Engineering, Washington University in St. Louis, Campus Box 1097, One Brookings Drive, St. Louis, Missouri 63130, USA

Abstract

We have developed spatially Fourier-encoded photoacoustic microscopy using a digital micromirror device. The spatial intensity distribution of laser pulses is Fourier-encoded, and a series of such encoded photoacoustic measurements allows one to decode the spatial distribution of optical absorption. The throughput and Fellgett advantages were demonstrated by imaging a chromium target. By using 63 spatial elements, the signal-to-noise ratio in the recovered photoacoustic signal was enhanced by $\sim 4\times$. The system was used to image two biological targets, a monolayer of red blood cells and melanoma cells.

Optical-resolution photoacoustic microscopy (OR-PAM) [1, 2], which provides the label-free detection of endogenous contrasts of optical absorption, has been used in many medical and biological applications [3–7]. The photoacoustic (PA) signal amplitude in OR-PAM depends on both the optical absorption coefficient of the target and the local light fluence. A common way to achieve high specific optical absorption (J/m^3) is to increase the local light fluence. However, the light fluence cannot exceed the damage threshold. For biological tissues, the maximum light fluence is usually further restricted by the ANSI safety standard [8] in *in vivo* experiments. As the resultant PA signal is always mingled with the random noise [9], low PA signal-to-noise ratio (SNR) translates into low contrast-to-noise ratio, which limits the visibility of features and the accuracy of functional imaging.

The SNR can be significantly improved by multiplexing. By delivering more energy to the target per laser pulse, multiplexing illumination gains a throughput (Jacquinot) advantage over single-element illumination. The signal of each individual element can be recovered by decoding the measured signal series. If the measurement contains only signal-independent noise sources, *e.g.*, random thermal noise from an ultrasonic transducer or random electronic noise in the amplifiers, then multiplexing approaches may enhance the SNR of the recovered signal, which is known as the Fellgett advantage.

Fourier and Hadamard transformations are commonly used in multiplexing methods [10–15]. Both have been widely used as spectral encoding mechanisms in applied spectroscopy [11, 12] as well as in many imaging modalities [13–15]. Multiplexing approaches can also

be implemented in the spatial domain. Recently, Rousseau and Blouin [16] demonstrated spatial Hadamard multiplexing in laser ultrasonics for the non-contact inspection of metal materials. A $2.8\times$ SNR improvement was achieved by using a one-dimensional Hadamard mask with 31 elements, each with an area of $100\times 100\text{ }\mu\text{m}^2$. However, this work cannot be readily implemented in microscopic biomedical imaging for two reasons. First, the utilization of the one-dimensional mask required scanning the target, resulting in a reduced imaging frame rate. Second, the lateral resolution ($100\text{ }\mu\text{m}$) was insufficient to distinguish micrometer-scale biological features.

In this letter, we present a spatially Fourier-encoded PAM (SFE-PAM) system using a digital micromirror device (DMD). This technique is inspired by the spectral Fourier-multiplexing method. The DMD was used as an optical encoder to produce time-domain discrete Fourier modulation patterns for each individual spatial element. Therefore, the SFE-PAM system can simultaneously deliver modulated light fluence to multiple locations of the target, thereby significantly improving the SNR of the PA signal over that of a single-element raster scan.

Herein we briefly review the Fourier multiplexing theory and derive the expected SNR enhancement for the SFE-PAM system. A 2D area of the target is divided into N elements, each with an absorption coefficient of $\mu_a(n)$ ($n = 1, \dots, N$). A conventional raster scanning requires N element-by-element measurements. For the n^{th} element, the generated PA A-line detected by the ultrasonic transducer, $v_r(n, t)$, can be written as

$$v_r(n, t) = s_r(n, t) + e(n, t), \quad (1)$$

where

$$s_r(n, t) = \mu_a(n) F_0(n) \hat{v}(t). \quad (2)$$

Here, the subscript r denotes raster scanning. $s_r(n, t)$ represents the time-resolved PA signal. $F_0(n)$ represents the incident light fluence. $\hat{v}(t)$ denotes the radiofrequency PA signal generated by an absorber with a unit specific optical absorption [*i.e.*, $\mu_a(n) F_0(n) = 1\text{ J/m}^3$ or another chosen unit]. $e(n, t)$ represents the random noise from the ultrasonic transducer and signal amplifiers, and its standard deviation is denoted by σ_r .

The principle of SFE-PAM is illustrated in Fig. 1. To satisfy the Nyquist sampling requirement, $2(N+1)$ Fourier-encoded patterns are imaged into the target [Fig. 1(a)]. The total PA signal amplitude is contributed by all N elements weighted by the Fourier-modulated light fluence. For the k^{th} measurement ($k = 0, \dots, 2N+1$), the Fourier-encoded radiofrequency PA signal, $v_f(k, t)$, can be written as

$$V_f(k, t) = \left(\sum_{n=1}^N \mu_a(n) F_0(n) \hat{F}_f(n, k) \right) \hat{v}(t) + e(k, t), \quad (3)$$

where the subscript f denotes Fourier encoding. $\hat{F}_f(n, k) = 1 + \cos[\pi nk / (N+1)]$ describes the fact that the laser pulse energy of each spatial element n is modulated by a distinct frequency

associated with the measurement index k [Fig. 1(b)]. The Fourier-encoded radiofrequency PA signals from successive $2(N+1)$ measurements are stacked to form a signal sequence.

This sequence is then decoded using the inverse Fourier transformation, which extracts the magnitude at each modulation frequency. The Fourier-decoded PA A-line, $\nu_f(m, t)$, can be written as

$$\nu_f(m, t) = s_f(m, t) + \varepsilon(m, t), \quad m = -N, \dots, N+1, \quad (4)$$

where

$$s_f(m, t) = \frac{1}{2(N+1)} \sum_{k=0}^{2N+1} \left\{ \left(\sum_{n=1}^N \mu_a(n) F_0(n) \hat{F}_f(n, k) \right) \hat{\nu}(t) \right\} \exp \left(i\pi \frac{mk}{N+1} \right), \quad (5)$$

and

$$\varepsilon(m, t) = \frac{1}{2(N+1)} \sum_{k=0}^{2N+1} e(k, t) \exp \left(i\pi \frac{mk}{N+1} \right). \quad (6)$$

Here, Eqs. (5) and (6) represent the signal and noise in the decoded PA A-line. N elements ($m = 1, \dots, N$) from Eq. (5) form an image, given by

$$s_f(m, t) = \frac{1}{2} \sum_{n=1}^N \mu_a(n) F_0(n) \delta_{mn} \hat{\nu}(t), \quad (7)$$

where δ_{mn} is the Kronecker delta function. Equation (7) shows that, each recovered element contains only half the value of the corresponding absorption coefficient, compared to the raster scan measurement [Fig. 1(c)]. The PA amplitudes of raster-scanned and Fourier-decoded PA A-lines are calculated by taking the absolute value of the Hilbert transforms of $S_r(n, t)$ and $S_f(n, t)$, respectively. Their ratio is found to be

$$\frac{|H\{s_f(n, t)\}|}{|H\{s_r(n, t)\}|} = \frac{1}{2}, \quad (8)$$

where $H\{\}$ denotes the Hilbert transformation.

In addition, we compared the standard deviation of the PA signal amplitude in raster-scanned and Fourier-decoded PA A-lines. The signal's standard deviation in the Fourier-decoded PA A-line, σ_f , is derived from Eq. (6):

$$\sigma_f = \frac{1}{\sqrt{2(N+1)}} \sigma_r. \quad (9)$$

However, to compensate for the unequal numbers of measurements, it is necessary to average the raster scan over two measurements because the Fourier encoding requires twice as many measurements as the raster scanning in general for $N \gg 1$. This reduces the

standard deviation in the raster-scanned PA A-line by a factor of $\sqrt{2}$, i.e., $\sigma_r' = \sigma_r / \sqrt{2}$. Equation (9) becomes

$$\sigma_f = \frac{1}{\sqrt{N+1}} \sigma_r'. \quad (10)$$

Thus, compared to the conventional raster scanning PAM, the Fourier encoding method suppresses the noise by a factor of $\sqrt{N+1}$.

The Fellgett advantage η is defined as the ratio of the SNR of the decoded PA A-line, $SNR_f(n, t) \equiv |H \{s_f(n, t)\}| / \sigma_f$, to that of the raster-scanned PA A-line, $SNR_r(n, t) \equiv |H \{s_r(n, t)\}| / \sigma_r'$. Combining Eqs. (8) and (10) gives

$$\eta \equiv \frac{SNR_f(n, t)}{SNR_r(n, t)} = \frac{\sqrt{N+1}}{2}. \quad (11)$$

The DMD-based SFE-PAM system (Fig. 2) employs a Nd:YVO₄ laser (SPOT 10-200-532, $\lambda = 532$ nm, Elforlight) as the illumination source. The generated laser pulses have a 2 ns pulse duration with a repetition rate of 10 kHz. The pulse energy is monitored by a photodiode detector (SM05PD1A, Thorlabs) to compensate for energy fluctuation. After expansion and collimation, the laser pulses impinge on the DMD (Discovery 4100, Texas Instruments) at an incident angle of 24° with respect to the surface normal. For each individual Fourier-modulation pattern, we use the two-dimensional Floyd-Steinberg error diffusion algorithm [17] to generate the corresponding DMD pattern, which is then imaged into the target through a system consisting of two 4f telescopes. Due to the limited spatial bandwidth of the imaging system, binary DMD patterns are converted to continuous grayscale images on the target. A 50 MHz ultrasonic transducer (V214-BB-RM, Olympus NDT Panametrics), placed confocally with the optical objective lens (Olympus, LUCPlanFLN 40×/0.60), is used to detect the PA signal. To fit the acoustic focal size of the transducer, the illumination field of view is set to be 35×35 μm^2 , with a lateral resolution of ~3.5 μm [18]. The optically determined lateral resolution limits the imaging depth to ~1 mm [2].

To demonstrate spatial Fourier-encoding in PAM, we first imaged a chromium target of the letters “WU”, made in-house by vacuum-deposition on a microscope coverslip substrate [Fig. 3 (a)]. The illumination field of view was evenly divided into 8×8 elements, in which $n = 1, \dots, 63$ elements were used for Fourier encoding. According to Eq. (11), the expected SNR enhancement is 4×. The average pulse energy was set to be 1.1 nJ per element. Compared to raster scanning [Fig. 3 (b)], the spatial Fourier encoding [Fig. 3 (c)] was experimentally shown to significantly increase the SNR of the data. Representative results of $v_r(n, t)$ and $V_f(m, t)$ are compared in Fig. 3 (d). While raster scanning yielded a PA A-line SNR of 4:1, Fourier encoding achieved an SNR of the Fourier-encoded data of 33:1. Consequently, the Fourier-decoded PA A-lines had a superior SNR. While the PA signal in most raster-scanned PA A-lines [Fig. 3(b)] was enshrouded in noise, the signal was clearly identifiable in the Fourier-decoded PA A-lines [Fig. 3 (e)]. Specifically, the PA A-lines of

the same element from both methods were analyzed [Fig. 3(f)]. Compared to the raster-scanned PA A-line, the signal amplitude of the Fourier-decoded PA A-line was approximately reduced by a factor of 2, as expected from Eq. (8). In addition, noise levels were quantified by calculating the standard deviation of the stacked raster-scanned [Fig. 3 (b)] and Fourier-decoded [Fig. 3 (e)] PA A-lines at 10 different time points in the same time window (0.3 – 0.5 μ s). Adjacent time points were chosen to be 20 ns apart to avoid noise correlation due to the limited bandwidth of the ultrasonic transducer. The calculated standard deviations at these 10 time points were averaged to compute the noise level. Compared to the raster-scanned PA A-lines, the averaged standard deviation in the Fourier-decoded PA A-lines was reduced by approximately 8 times. Thus, the SNR was improved by ~ 4 times with spatial Fourier encoding, which agrees well with the value expected from Eq. (11).

A volumetric image of the target's optical absorption was produced by allocating each individual PA A-line in the stack to the corresponding spatial element position. Then, this volumetric 3D image was rendered as a 2D maximum amplitude projection (MAP) image along the depth direction. The PA image of the letters "WU" demonstrated that the Fourier encoding had significantly enhanced image quality compared to the raster scanning (Fig. 4). When the transient PA A-line peak had a signal level comparable with the detector's noise in raster scanning, the target could not be accurately resolved. In contrast, the Fourier-decoded image clearly depicted the optical absorption distribution over the entire target because of the enhanced SNR.

To test the SFE-PAM system performance with biological contrasts, we imaged red blood cells (RBCs) and melanoma cells. The average pulse energy was set to be 2.8 nJ per element. A monolayer RBC target was prepared by spreading a drop of whole bovine blood (910-250, Quad Five) across a coverslip. Due to low PA SNR, the raster scanning resulted in a low quality image [Fig. 5 (a)]. In contrast, the Fourier encoding method could distinguish five sparsely distributed RBCs in the field of view [Fig. 5 (b)]. In addition, B 16 melanoma cells fixed on a coverslip were imaged using the raster scanning and Fourier encoding methods. Akin to the results from the RBC target, while no features could be identified using the raster scanning [Fig. 5 (c)], the cellular boundary was clearly revealed by the PA image obtained by the Fourier encoding [Fig. 5 (d)]. These results demonstrated that the PA image quality was considerably improved by using the Fourier-encoding method.

Although implemented in OR-PAM, the conceptual design of spatial Fourier encoding is applicable to many other imaging modalities, *e.g.*, fluorescent microscopy. Compared to traditional interferometry-based Fourier modulation approaches, the present approach uses a DMD as a spatial Fourier encoder. Avoiding a moving reference mirror, the SFE-PAM system acquires images without mechanical movement, making the system more stable for practical applications. In comparison to a laser illumination array [19], the present system requires only a single laser source and gives users the flexibility to control the number of used spatial elements according to the application.

In summary, we report the first experimental demonstration of a SFE-PAM system based on a DMD, which is used to modulate the spatial light distribution of the laser beam. Each

spatial element of the target is illuminated by modulated light fluence with a different frequency. The spatial optical absorption distribution is recovered by decoding a series of Fourier-encoded PA measurements. Compared to raster scanning with the same number of measurements, the SFE-PAM system enables more energy-efficient delivery of the laser illumination. In addition, this system possesses the Fellgett advantage, in terms of PA SNR, in the Fourier-decoded PA A-lines. The enhanced SNR benefits PA images by increasing image contrast-to-noise ratio and target identifiability. The SFE-PAM system is an attractive tool for the accurate PA measurement of biological targets with low optical absorption coefficients or low damage threshold.

Acknowledgments

The authors thank Lijun Ma, Yong Zhou, Chi Zhang, and Lei Li for helpful discussions, and Professor James Ballard for close reading of the manuscript. This work was sponsored in part by National Institutes of Health grants DP1 EB016986 (NIH Director's Pioneer Award), R01CA134539, R01CA157277, and R01 CA159959. L. W. has a financial interest in Microphotoacoustics, Inc. and Endra, Inc., which, however, did not support this work.

References

1. Maslov K, Zhang HF, Hu S, Wang LV. Optical-resolution photoacoustic microscopy for in vivo imaging of single capillaries. *Opt. Lett.* 2008; 33:929–931. [PubMed: 18451942]
2. Wang LV, Hu S. Photoacoustic Tomography: In Vivo Imaging from Organelles to Organs. *Science.* 2012; 335:1458–1462. [PubMed: 22442475]
3. Paproski RJ, Forbrich AE, Wachowicz K, Hitt MM, Zemp RJ. Tyrosinase as a dual reporter gene for both photoacoustic and magnetic resonance imaging. *Biomed. Opt. Express.* 2011; 2:771–780. [PubMed: 21483602]
4. Jiao S, Jiang M, Hu J, Fawzi A, Zhou Q, Shung KK, Puliafito CA, Zhang HF. Photoacoustic ophthalmoscopy for in vivo retinal imaging. *Opt. Express.* 2010; 18:3967–3972. [PubMed: 20389409]
5. Li R, Slipchenko MN, Wang P, Cheng J-X. Compact high power barium nitrite crystal-based Raman laser at 1197 nm for photoacoustic imaging of fat. *Journal of Biomedical Optics.* 2013; 18:040502–040502. [PubMed: 23536057]
6. Gao L, Wang L, Li C, Liu Y, Ke H, Zhang C, Wang LV. Single-cell photoacoustic thermometry. *Journal of Biomedical Optics.* 2013; 18:026003–026003.
7. Liang J, Zhou Y, Maslov KI, Wang LV. Cross-correlation-based transverse flow measurements using optical resolution photoacoustic microscopy with a digital micromirror device. *Journal of Biomedical Optics.* 2013; 18:096004–096004. [PubMed: 24002191]
8. Laser Institute of America. American National Standard for Safe Use of Lasers. Laser Institute of America; 2007.
9. Sivaramakrishnan M, Maslov K, Zhang HF, Stoica G, Wang LV. Limitations of quantitative photoacoustic measurements of blood oxygenation in small vessels. *Physics in Medicine and Biology.* 2007; 52:1349. [PubMed: 17301459]
10. Graff DK. Fourier and Hadamard: Transforms in Spectroscopy. *Journal of Chemical Education.* 1995; 72:304.
11. de. Haseth, JA.; Griffiths, Peter R. *Fourier Transform Infrared Spectrometry.* John Wiley & Sons, Inc.; 2006.
12. Hammaker RM, Bohlke AP, Jarvis JM, Tate JD, White JS, Paukstelis JV, Fateley WG. Recent developments in Hadamard transform Raman spectrometry. 1990:124–134.
13. Eberhardt KW, Hunkeler A, Meier U, Tharian J, Mouaziz S, Boero G, Brugger J, Meier BH. Two-dimensional magnetic resonance force microscopy using full-volume Fourier and Hadamard encoding. *Physical Review B.* 2008; 78:214401.

14. Wang Y, Maslov K, Wang LV. Spectrally encoded photoacoustic microscopy using a digital mirror device. *Journal of Biomedical Optics*. 2012; 17:0660201–0660205.
15. Hanley, Verveer, Arndt J, Jovin. Three-dimensional spectral imaging by Hadamard transform spectroscopy in a programmable array microscope. *Journal of Microscopy*. 2000; 197:5–14. [PubMed: 10620143]
16. Rousseau G, Blouin A. Hadamard multiplexing in laser ultrasonics. *Opt. Express*. 2012; 20:25798–25816. [PubMed: 23187397]
17. Liang J, Kohn JRN, Becker MF, Heinzen DJ. 1.5% root-mean-square flat-intensity laser beam formed using a binary-amplitude spatial light modulator. *Appl. Opt.* 2009; 48:1955–1962. [PubMed: 19340151]
18. Liang J, Zhou Y, Winkler AW, Wang L, Maslov KI, Li C, Wang LV. Random-access optical-resolution photoacoustic microscopy using a digital micromirror device. *Opt. Lett.* 2013; 38:2683–2686. [PubMed: 23903111]
19. Steckenrider JS, Murray TW, Wagner JW, John J, Deaton B. Sensitivity enhancement in laser ultrasonics using a versatile laser array system. *The Journal of the Acoustical Society of America*. 1995; 97:273–279.

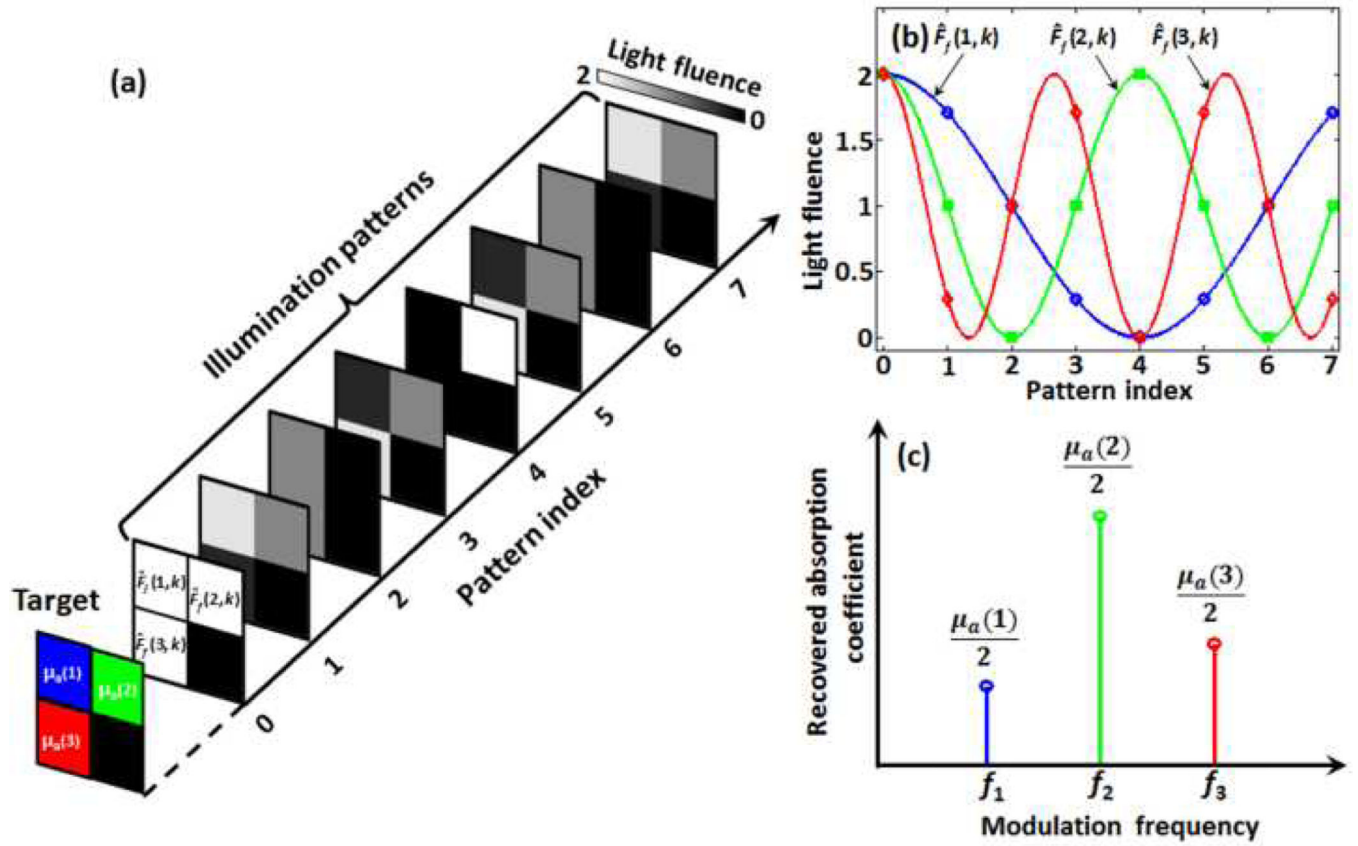


Fig 1.

Principle of spatially Fourier-encoded photoacoustic microscopy. A 3-pixel encoding of $(F_f^{\wedge}(n,k), n = 1, \dots, 3)$ is illustrated. (a) The target is illuminated by a series of patterns. The laser fluence of each element in the pattern is modulated at a different frequency. (b) Light fluence of each element versus illumination pattern index. (c) Absorption coefficients recovered with Fourier decoding.

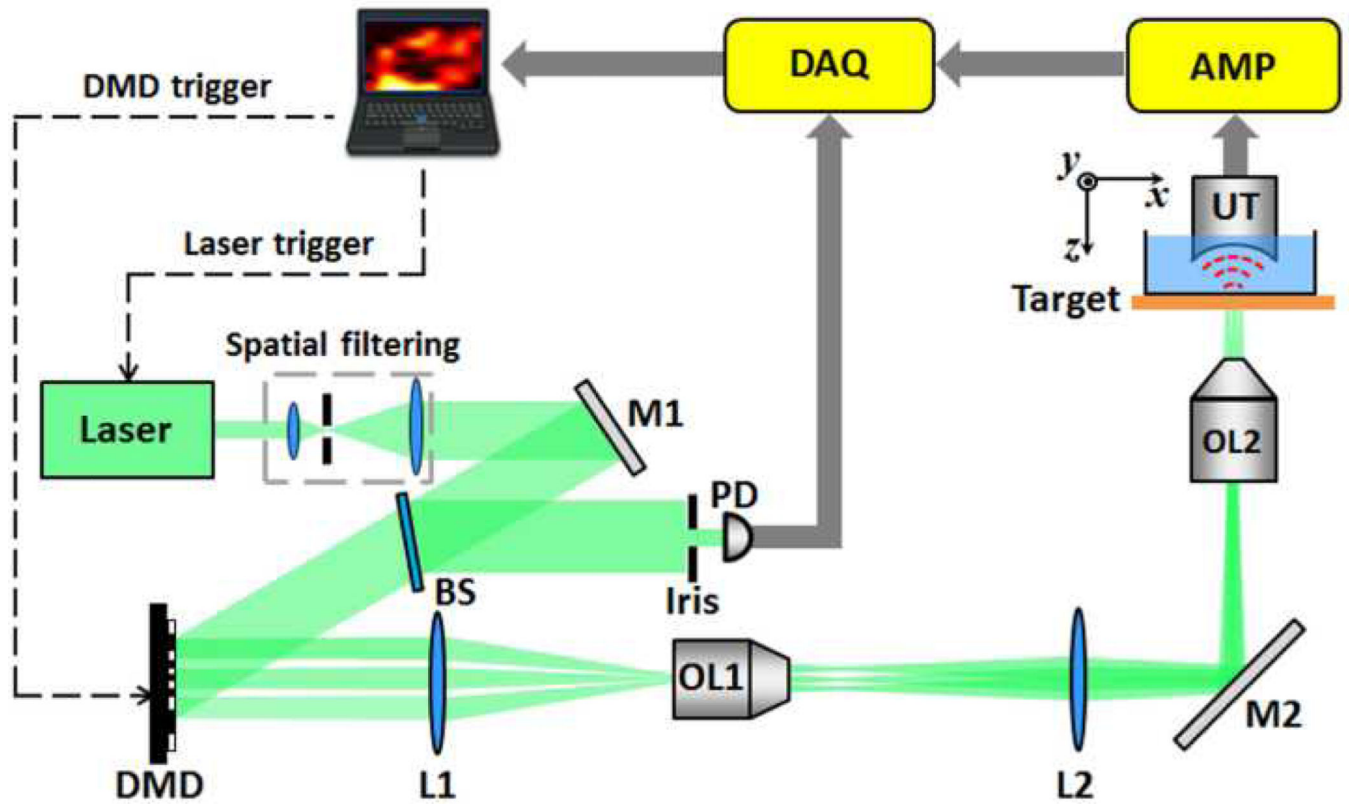


Fig 2.

Schematic overview of the spatially Fourier-encoded photoacoustic microscopy system (not to scale). AMP, signal amplifiers and filters; BS, beam sampler; DAQ, data acquisition system; DMD, digital micromirror device; L1–L2, lenses; M1–M2, mirrors; OL1, objective lens (Mitutoyo, M PLAN APO 10×/0.28); OL2, objective lens (Olympus, LUCPlanFLN 40×/0.60); PD, photodiode detector; UT, ultrasonic transducer.

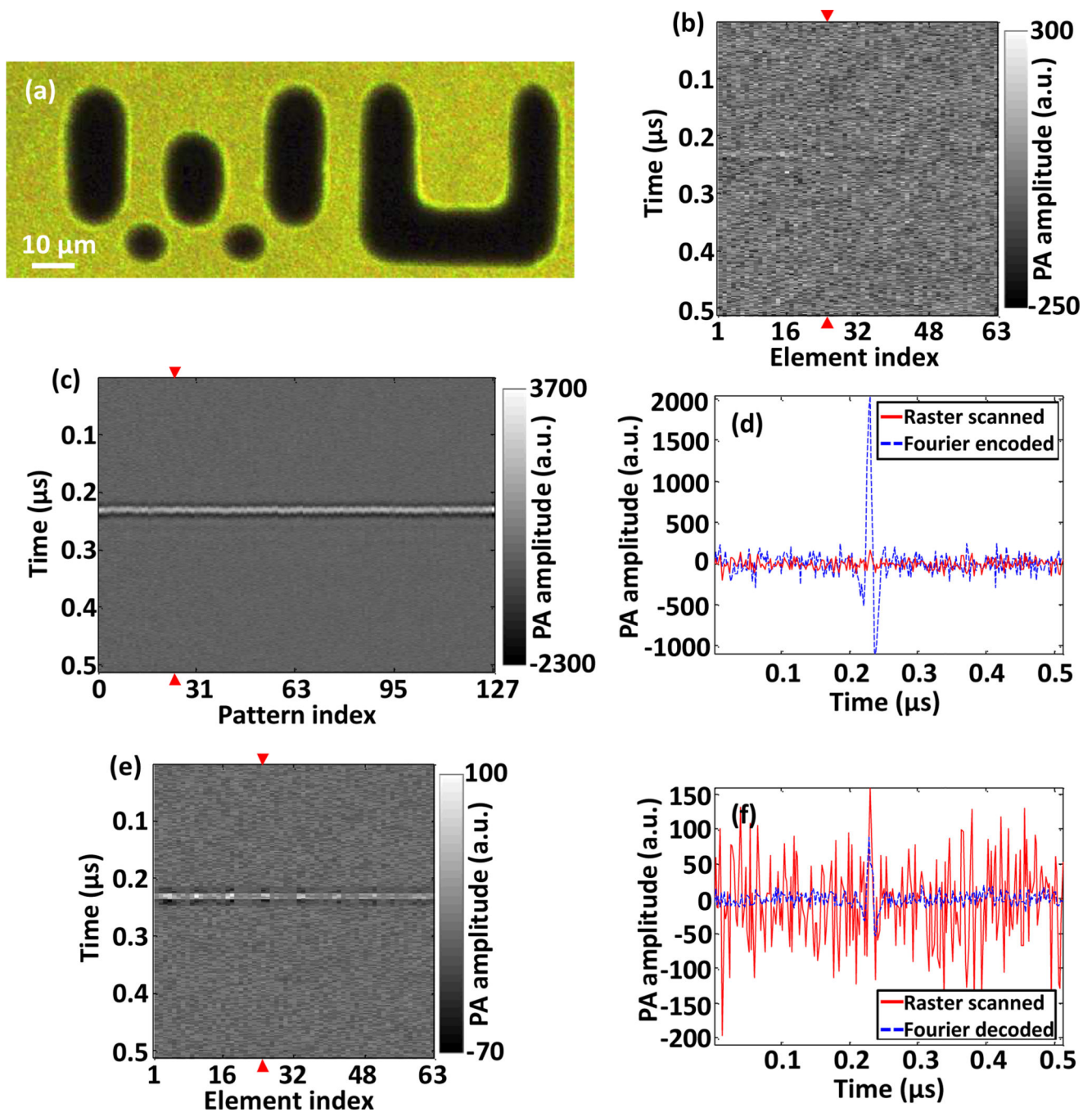


Fig 3.

(a) Photograph of a chromium target of the letters "WU". (b) Stack of PA A-lines of the letter "U" acquired with raster scanning. The measurement result from the raster scanning was acquired twice and averaged to match the total number of signals acquired with the Fourier encoding. (c) Stack of radiofrequency PA signals of the letter "U" acquired by Fourier encoding. (d) Comparison of PA signals (between red triangles) in (b) and (c). (e) Stack of Fourier-decoded PA A-lines of the letter "U". (f) Comparison of PA A-lines (between red triangles) in (b) and (e).

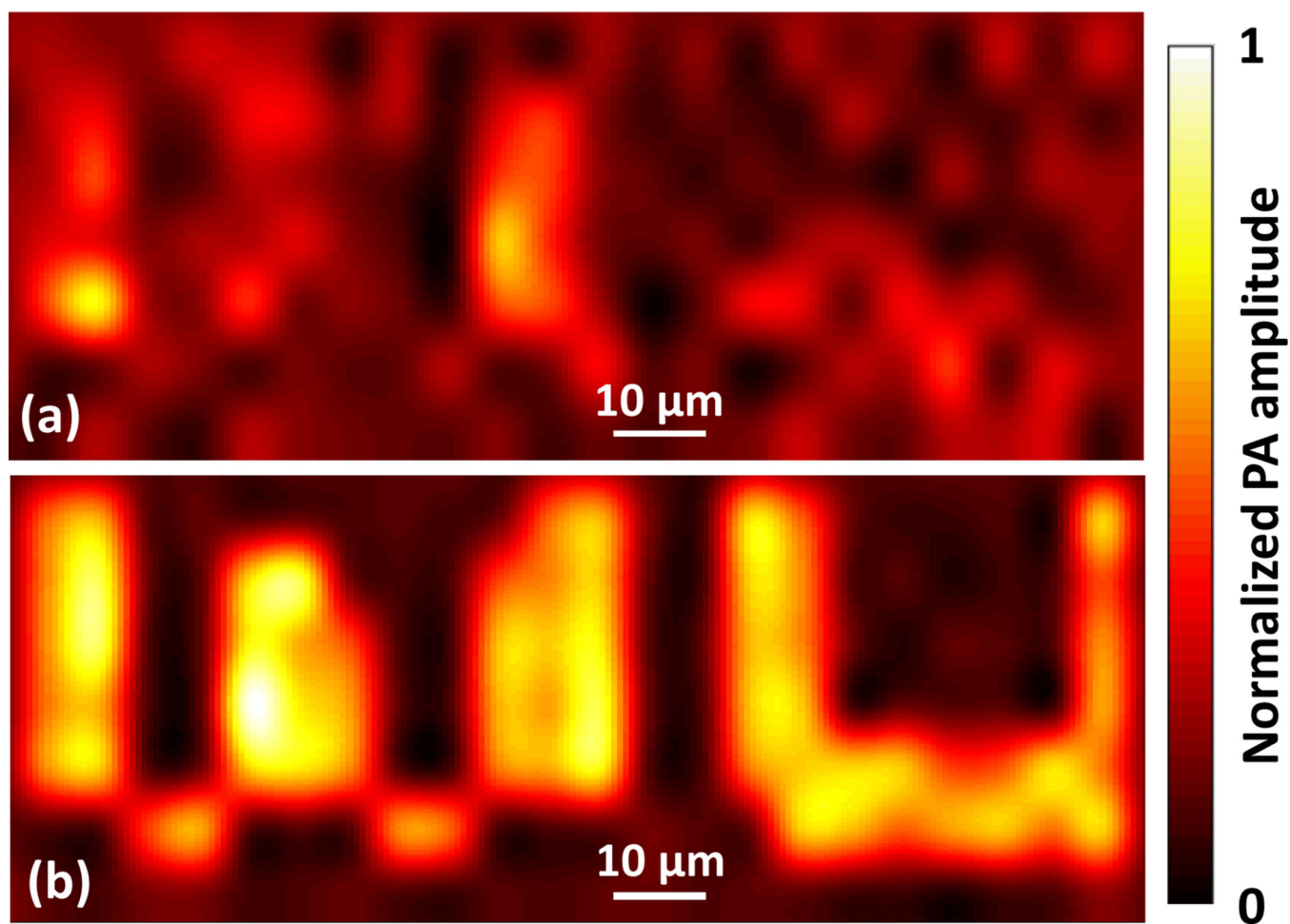


Fig 4.
PA images of a "WU" logo made of deposited chromium acquired by (a) raster scanning and (b) Fourier encoding.

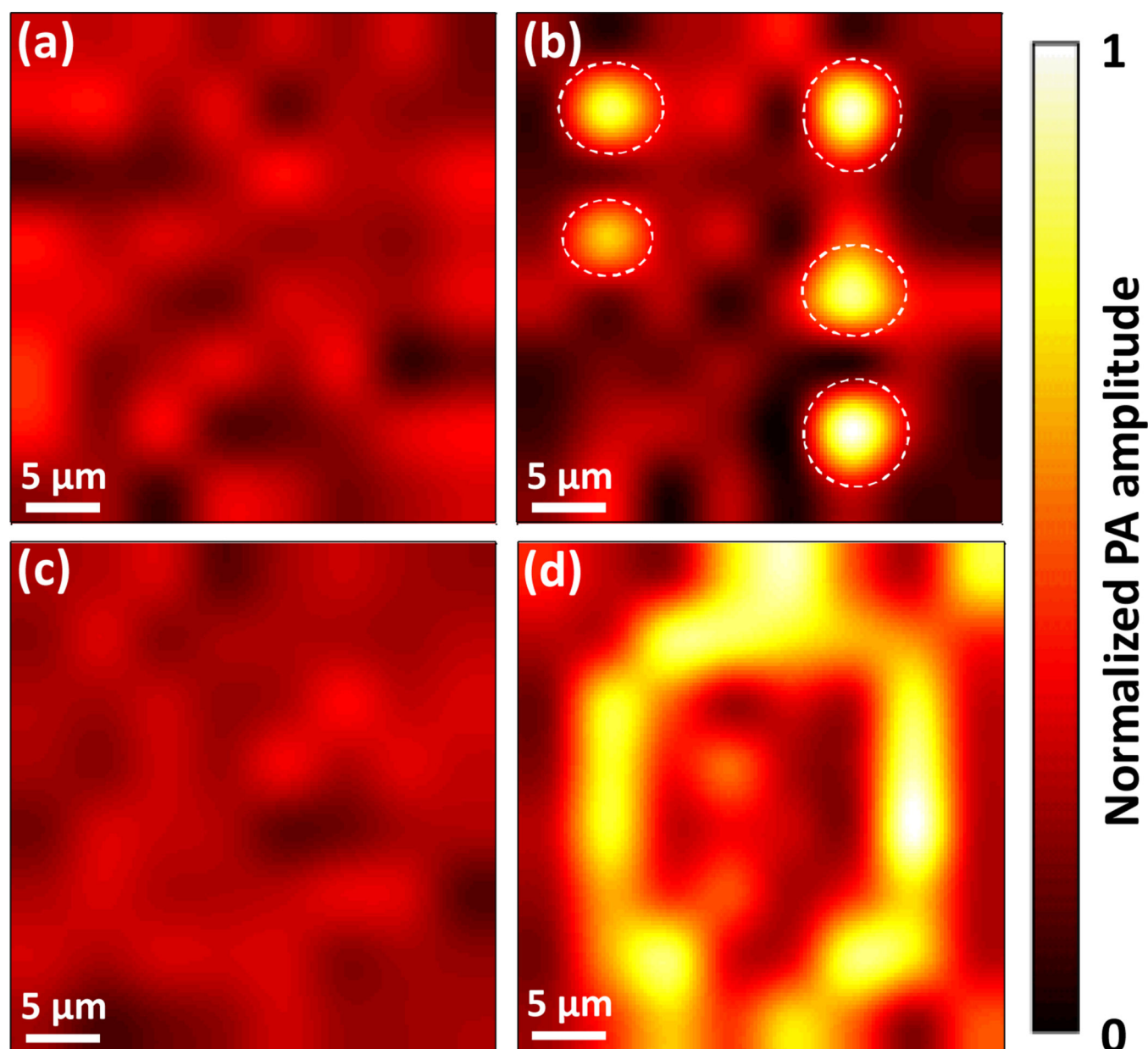


Fig 5. Demonstration of spatial Fourier-encoding method in biological targets. PA images of monolayer RBCs acquired by (a) raster scanning and (b) Fourier encoding. RBCs are identified by white dashed circles. A melanoma cell was also imaged using (c) raster scanning and (d) Fourier encoding.